CONF-8510173--39

FINAL

NDE OF STAINLESS STEEL AND ON-LINE LEAK MONITORING OF LWRs*

D. S. Kupperman
Materials Science and Technology Division
T. N. Claytor
Components Technology Division

ARGONNE NATIONAL LABORATORY
Argonne, Illinois 60439

T. Mathieson and D. W. Prine
GARD, Inc.
Division of Chamberlain National
Niles, Illinois 60648

CONF-8510173--39

TI86 004052

October 1985

To be published in the Proceedings of the 13th Water Reactor Safety Research Information Meeting, October 22-25, 1985, Gaithersburg, MD, sponsored by the Nuclear Regulatory Commission.

*Work supported by the U.S. Nuclear Regulatory Commission, Office of Nuclear Regulatory Research.

NDE OF STAINLESS STEEL AND ON-LINE LEAK MONITORING OF LWRs*

D. S. Kupperman (MST) and T. N. Claytor (CT)
Argonne National Laboratory
Argonne, Illinois 60439
and
T. Mathieson, and D. W. Prine
GARD, Inc.
Division of Chamberlain National
Niles, Illinois 60648

ABSTRACT

The GARD/ANL acoustic leak detection system is under evaluation in the laboratory. Results of laboratory tests with simulated acoustic leak signals and acoustic signals from field-induced intergranular stress corrosion cracks (IGSCCs) indicate that cross-correlation techniques can be used to locate the position of a leak.

Leaks from a 2-in. ball valve and a flange were studied and compared with leaks from IGSCCs and fatigue cracks. The dependence of acoustic signal on flow rate and frequency for the valve and the flange was comparable to that of fatigue cracks (thermal and mechanical) and different from that of IGSCCs.

An informal workshop on NDE of pipes with weld overlays was held at ANL. Personnel from four research institutions and one utility attended the workshop. Two pipe-to-endcap weldments with overlays were examined. Because the amount of cracking in the specimens was limited, the emphasis was on trying to understand the nature of crack overcalling. We concluded that it is difficult to inspect pipes with overlays because of unpredictable beam distortion due to the overlay and the absence of effective reference pipes. The use of 1-MHz longitudinal angle-beam probes rather than shear-wave probes may facilitate inspection of such pipes.

Four 60-mm-thick cast stainless steel plates with microstructures ranging from equiaxed to primarily columnar grains have been examined with ultrasonic waves. We have found that the longitudinal velocity of sound and the ratio of longitudinal to shear velocity as a function of position can be used to characterize the crystallographic texture. We have also found that the beam skewing that occurs in columnar (but not equiaxed) structures is strong enough so that measurements of probe separation at maximum received signal intensity for 45° shear-wave pitch-catch transducers can be correlated with microstructure.

*Work supported by the U.S. Nuclear Regulatory Commission, Office of Nuclear Regulatory Research.

A. Background and Objectives

1. On-Line Leak Monitoring of LWRs

No currently available single leak-detection method combines optimal leakage detection sensitivity, leak-locating ability, and leakage measurement accuracy.[1] For example, while quantitative leakage determination is possible with condensate flow monitors, sump monitors, and primary coolant inventory balance, these methods are not adequate for locating leaks and are not necessarily sensitive enough to meet regulatory-guide goals. The technology is available to improve leak detection capability at specific sites by use of acoustic monitoring or moisture-sensitive tape. However, current acoustic monitoring techniques provide no source discrimination (e.g., to distinguish between leaks from pipe cracks and valves) and no flow-rate information (a small leak may saturate the system). Moisture-sensitive tape provides neither quantitative leak-rate information nor specific location information other than the location of the tape; moreover, its usefulness with "soft" insulation needs to be demonstrated. Hence, leak detection techniques need further improvement in the following areas: (1) identifying leak sources through location information and leak characterization, to eliminate false calls; (2) quantifying and monitoring leak rates; and (3) minimizing the number of installed transducers in a "complete" system through increased sensitivity.

The objectives of the leak detection program are to (a) develop a facility to evaluate acoustic leak detection (ALD) systems quantitatively and (b) assess the effectiveness of field-implementable ALD systems. The program will establish whether meaningful quantitative data on leak rates and location can be obtained from acoustic signatures of leaks due to intergranular stress corrosion cracks (IGSCCs) and fatigue cracks, and whether these can be distinguished from other types of leaks. It will also establish calibration procedures for acoustic data acquisition and show whether advanced signal processing can be employed to enhance the adequacy of ALD schemes.

2. NDE of Stainless Steel

The present ASME Code Sections V and XI, which pertain to ultrasonic testing procedures for ferritic weldments, do not appear to be adequate for cast stainless steel (CSS) or for IGSCCs in austenitic stainless steel (SS) piping. Although the probability of detecting IGSCCs under field conditions has increased since the issuance of NRC IE Bulletins 83-02 and 82-03, the detection of these cracks is still difficult. Many cracks are missed during ultrasonic in-service inspection (ISI) and are detected only when leakage occurs.

The objectives of the ultrasonic NDE program are to (a) assess methods for characterizing the microstructure of CSS to determine ISI reliability, (b) evaluate the ultrasonic inspection problems associated with weld overlays, and (c) assess problems in trying to distinguish intergranular cracks from geometrical reflectors.

B. Technical Progress in Acoustic Leak Detection

1. Acoustic Signals from a Leaking Valve and Flange

The stem of a 2-in. ball valve (Whitey Co. "F6C") was scratched with a tool engraver along the stem axis to create a fluid leakage path. By varying the packing load, the flow rate could be varied from 0.004 to 0.3 gal/min. One side of the valve was joined to a piece of 2-in. pipe about 1 m long, and the other side was connected to a 1/4-in.-diam (6-mm) SS line that fed high-pressure (1100 psi), high-temperature (to 500°F) water to the valve body. Heaters were wrapped around the valve to maintain the desired temperature. An AET-375 transducer was attached to a 3-mm-diam waveguide which was screwed into a small hole in the valve body. Although the valve was not integrated into the 10-in. Schedule 80 piping of the ALD facility as crack specimens have been, it was still possible to compare the acoustic leak signals from the valve with signals from leaking cracks. This was accomplished by injecting a controlled, electronically generated acoustic signal into the valve body and then into the pipe run at the location of one of the cracked pipe sections. The difference in detected signal at two points for the same injected signal was noted. This provided a multiplication factor for use in estimating the acoustic signal that would be detected 1 m from the valve leak if the valve were integrated into the pipe run. This method was reproducible and led to a correction of 14 dB (i.e., the acoustic signal from the leaking valve body is 14 dB more intense than it would be if the valve were integrated into the pipe run and the signal detected at a distance of 1 m).

Tests were also run on a leaking flange. Figure 1 shows the configuration and dimensions of the flange, which was placed over a section of the ALD pipe run. Leaks were generated by placing a small wire segment underneath the O-ring and varying the load. The fluid temperature and pressure ranged from 350 to 500°F (177 to 260°C) and 1000 to 1100 psi (7.0 to 7.7 MPa), respectively. Flow rates ranged from 0.01 to 1.0 gal/min (0.6 to 63 cm^3/s).

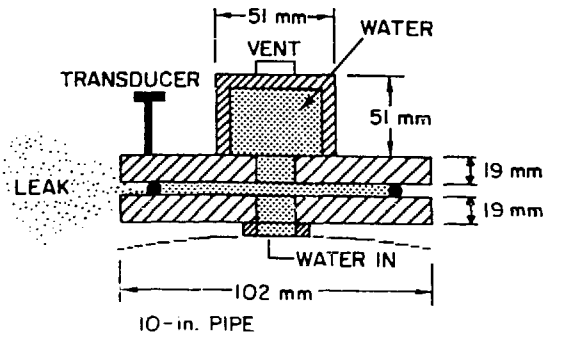

Fig. 1. Schematic Representation of Flange Leak.

The normalized acoustic data for both valve and flange are presented along with data from various cracks in Fig. 2. Although there is considerable scatter in the valve and flange leak data, the trend is clear. The acoustic signals from leaking IGSCCs are less dependent on flow than those from other types of leaks. In addition, over the range of flow rates examined, the signal amplitudes for the valve and flange are of the same order of magnitude as those for thermal- and mechanical-fatigue cracks.

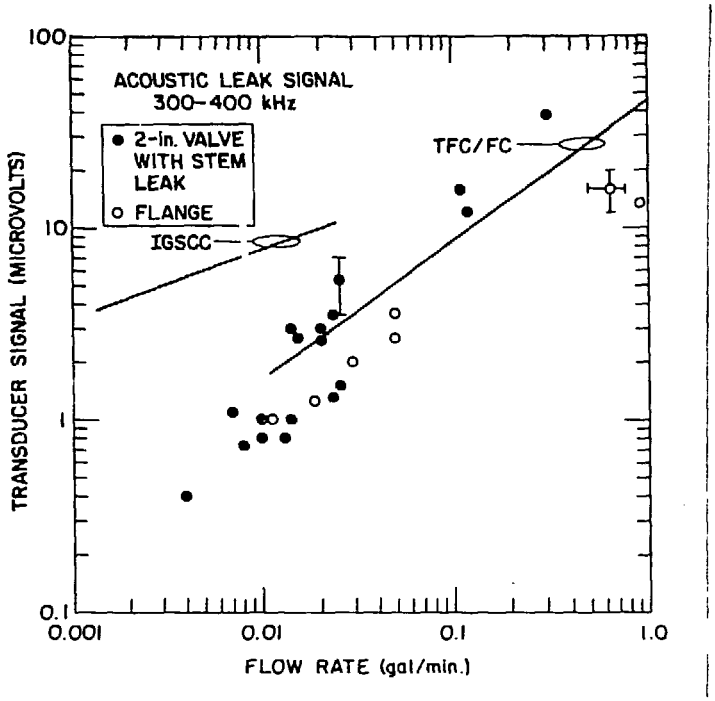

Fig. 2. Acoustic Signal vs Flow Rate for Leaks from IGSCCs, Thermal-Fatigue Cracks (TFC), Mechanical-Fatigue Cracks (FC), Flange, and Valve Stem. All data were normalized to an AET-375 Transducer (300-400 kHz frequency range) on a 3-mm-diam waveguide 1 m from the leak.

We have also found that for the same signal amplitude in the 300-400 kHz range, there is relatively more low-frequency signal for the valve and flange than for the IGSCC. A similar result was found for fatigue cracks relative to IGSCCs. This result supports the argument that, at least for flow rates of less than 1 gal/min, it may be possible to distinguish IGSCC leaks from other leaks by comparing the ratio of acoustic signal intensity in low (50-150 kHz)- and high (300-400 kHz)-frequency windows.

2. Evaluation of the Digital Continuous Acoustic Monitoring System

The digital continuous acoustic monitoring system (DCAMS), shown in Fig. 3, consists of two LeCroy Transient Data recorders, a Camac Dataway, and a Dual 83/20 Unix-based computer. Signals from acoustic emission trans-

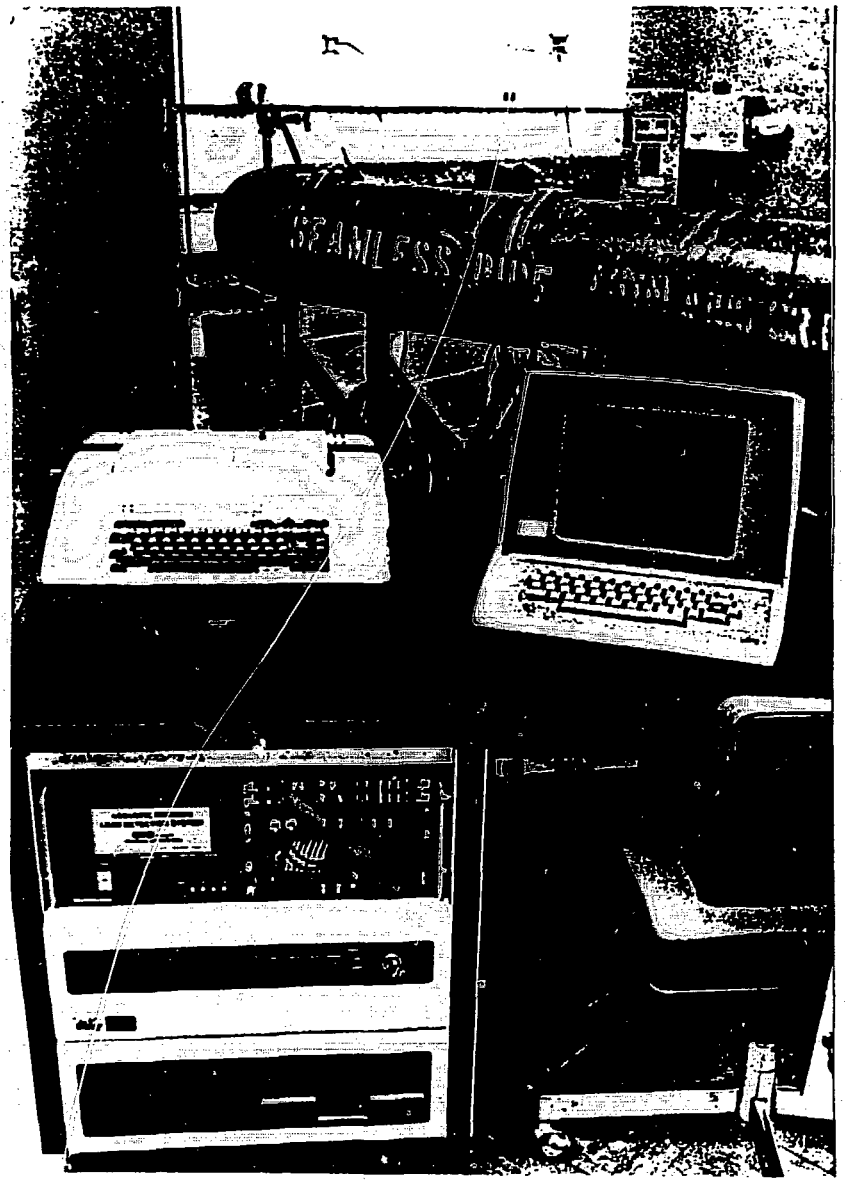

Fig. 3. Photograph of Digital Continuous Acoustic Monitoring System for Leaks.

ducers are amplified by Tektronix AM502 amplifiers, passed through Khrone-Hite filters and a signal conditioner for gain control, and subsequently sent to the transient recorders and computer. The system has a high-resolution monitor and an English-language command syntax. At a sampling rate of 500 kHz and 8000 points per channel per acquisition, 16 ms of continuous acoustic data can be recorded per capture. The system is capable of storing about 10 MB of data. For a two-channel system, this implies that at 16,000 points per acquisition (8000 per channel), 160 data acquisitions can be

stored. The radio frequency data can then be analyzed to provide rms data, frequency spectra, and cross-correlation functions including averaging of correlograms. A considerable amount of data can be stored and recalled at a future time for additional analysis. DCAMS has been tested by injecting known signals directly into the signal conditioner inputs. These signals were the outputs of standard signal generators and a time-delayable random noise generator. These tests proved that the hardware reception and software processing of the DCAMS were performing their required functions.

Subsequent tests of signals received through transducer excitation from acoustic activity in a section of the ALD facility did not yield results of such unambiguous quality. In the simplest case, capture of controlled single pulses and subsequent cross-correlation yielded unexpected time difference lags. When the transducers were arranged so that acoustic waves did not travel across elbows in the test loop, the location results became more consistent.

Further tests of the capture and cross-correlation of single acoustic pulses revealed that leak-locating ability requires more similarity between the two sampled signals than is easily achieved on the test loop. In addition, it was found that when the receiving transducers were so placed and clamped as to produce similar-appearing envelopes for the two sampled waveforms, the locational accuracy improved.

One possible cause of the observed locational inconsistencies is phase perturbation introduced in the signal by the transfer function of the pipe, coupling, and transducer combination. If this is the case, the use of demodulation should yield more consistent results at the cost of resolution. A demodulator circuit developed by ANL was added to the DCAMS signal input hardware to test this hypothesis. Location accuracy was as good as the best results without the demodulator, but reliability did not improve. More detailed tests showed that the mismatch of frequency response between the DCAMS signal conditioner and the demodulator was contributing to this unreliability. Consequently, a software demodulator was written and tested. This software demodulator works better than the hardware demodulator and, in addition, demonstrates exactly how sensitive locational accuracy is to the similarity of signal envelope profiles.

After the system was modified as described above, several experiments were carried out to illustrate the system capability, with encouraging results. In one, an electronic pulser and two AET-375 receivers were used to demonstrate the enhancement of location capability with demodulated acoustic signals. A program was written to allow the system operator to rectify and smooth the captured and digitized radio frequency signals. Correct location information was generated with receivers separated by $\sim$1.5 m. In a second experiment, FAC 500-kHz broadband and AET-375 resonance receivers were attached to the ends of the pipe run (a separation distance of 10 m). A continuous noise source was placed at several different locations for these tests. All tests were carried out with radio frequency signals and with the pipe empty. In each of these tests, correlograms were averaged. Unambiguous

location of the source was indicated in all trials. Tests without averaging showed considerable variation in source location. In another successful test, AET-375 probes were attached to waveguides at the ends of the pipe run. Nine correlograms were averaged, but in this case the waveguides were moved slightly in a circumferential direction before each radio frequency signal was captured. This produced a spatial average and resulted in the best S/N ratio for location yet achieved. The results of frequency spectrum analysis indicate that acoustic waves at frequencies greater than 250 kHz are severely damped over the distances involved in the current tests (10 m). As a result, cross-correlation analysis can be effective at radio frequency signal capture rates of 500 kHz (2 μs between capture points). The consequence of this is that the 10-m transducer separation can be represented on the monitor to facilitate the visual interpretation of source location information. The results of experiments with waveguides on the ends of the pipe run are seen in Fig. 4. The movement of the correlation peak with movement of the electronic noise source is clearly evident.

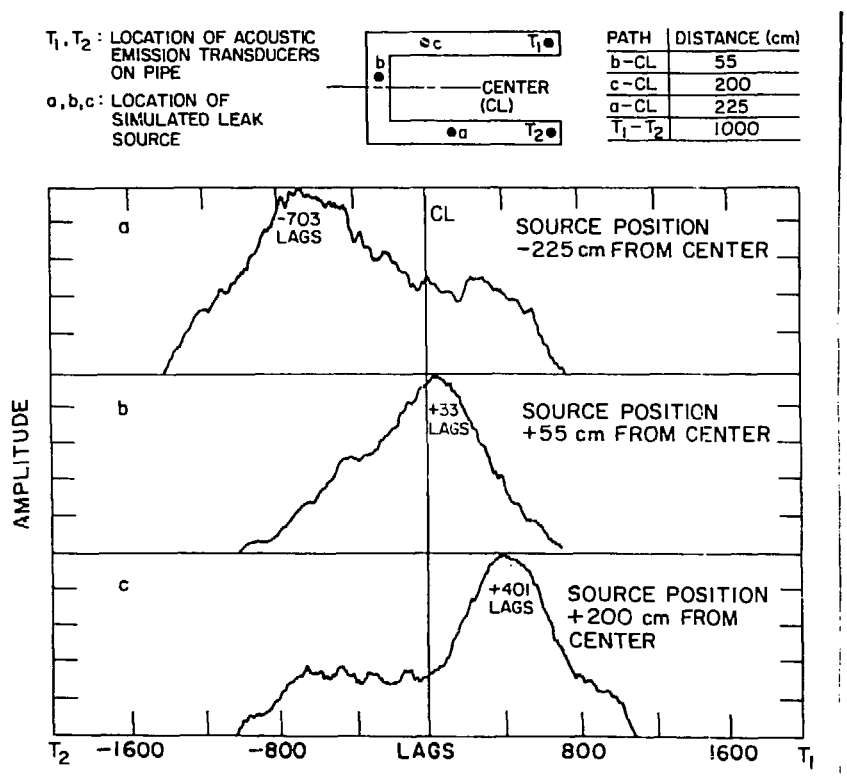

Fig. 4. Movement of Spatially Averaged Cross-Correlation Peak with Changes in Location of Continuous Acoustic Source. The waveguides on which the transducers are mounted are moved slightly in a circumferential direction after each correlogram is generated.

A laboratory test has been carried out to help evaluate the capability of DCAMS to locate an actual leaking field-induced IGSCC by averaging cross-correlation functions. Two AET-375 receivers were placed on waveguides, 164 cm apart; one 61 cm, the other 103 cm from IGSCC #1. A 0.003-gal/min leak was generated from IGSCC #1 at 504°F and 1000 psi. With the flow off and electronic filters passing 150- to 500-kHz signals, the electronic background noise levels were 31 and 42 mV, respectively. With the flow on, the signal amplitudes increased to 51 and 68 mV. The sampling rate for these tests was 500 kHz (2 μs between data points). Nine correlograms were averaged. In generating these correlograms, one of the two waveguides was moved circumferentially (about 60°) before the next waveform was captured. This averaging technique permitted a leaking field-induced IGSCC to be located, for the first time, by cross-correlation techniques. The results are shown in Fig. 5. The correlogram peak is shifted 266 μs (133 lags at 2 μs per lag) from the center. This corresponds to a difference in path length of about 80 cm, based on the velocity of shear waves in steel. This result agrees in both sign and order of magnitude with the actual difference of 42 cm. The location accuracy of the system, however, has yet to be determined. Similar tests carried out with an electronic leak signal indicated that location accuracy improves with signal amplitude. This result suggests that larger leaks would be located with greater reliability.

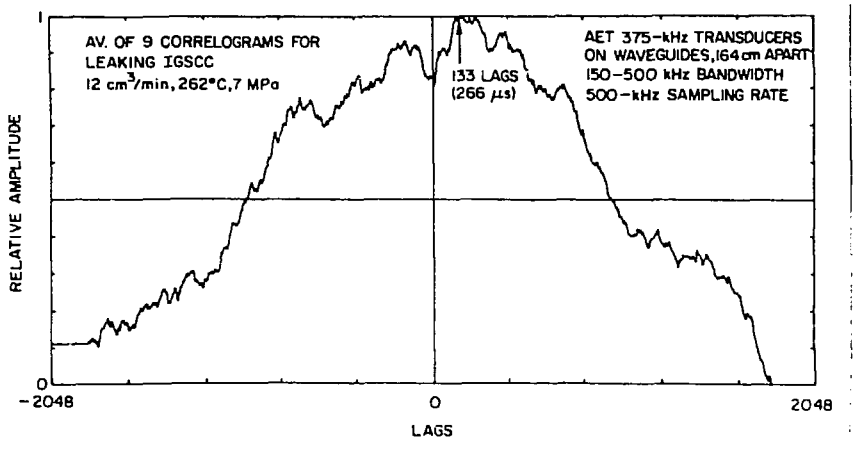

Fig. 5. Cross-Correlation Function (Average of Nine Correlograms) for Leaking Field-induced IGSCC.

Only three different circumferential positions for each waveguide were required to acquire the nine correlograms. Thus, the averaging procedure could be carried out with three transducer/waveguide systems at each monitoring site. It may be possible to carry out cross-correlation analysis with one transducer at each monitoring site, if larger leaks are present. Future tests will address this point.

An experiment was carried out to demonstrate that the cross-correlation analysis could be carried out with both empty and water-filled pipes. Correlograms were obtained from acoustic pulses generated between transducers located in the section of the pipe that can be filled with water. The probes were separated by about 1.5 m. With the pipe empty, correct location information was obtained from the time lag and the estimated velocity of surface waves in steel. With the pipe filled with water, equally accurate correlograms were obtained. Correct location of the pulser in the latter case was obtained from the time lag and the known velocity of L-waves in water. This demonstrates that the dominant signals received by the acoustic emission transducers at a separation of 1.5 m were from acoustic waves propagating through the water in the pipe.

During the current reporting period, several options for improving the DCAMS graphics were considered. After viewing several demonstrations, we purchased a Lear Siegler ADM 3 graphics terminal with a factory-installed Selanar Graphics (SG) 305 board. This terminal can emulate most of the Tektronix 4010/4014 features and can provide additional features in the "Selanar Native" mode. Table 1 shows the actual and addressable screen boundaries for the two modes.

TABLE 1. Actual and Addressable Screen Boundaries for the Modified ADM 3 Terminal

Mode	Actual Dot Resolution		Viewable Area		Addressable Area	
	x	y	x	y	x	y
Tektronix	644	247	1024	780	1024	1024
				or		or
			4096	3120	4096	4096
Selanar Native	644	247	2576	991	±32384	±32384

The viewable area of the Tektronix 4014 mode is "mapped into" available resolution on the 305 screen within its visible area. The aspect ratio is made proportional so that circles appear as circles in the Tektronix mode.

In the native mode, the horizontal and vertical gain factors can be changed to any value in the range from 0.004 to 256 times normal to vary the aspect ratio. Changes in the gain can also be used for drawing ellipses of different eccentricities with the arc/circle generation features. Once the gain factors are set in the native mode, they are also implemented in the Tektronix mode.

Full upper- and lowercase ASCII and APL character sets are included in the Tektronix alphanumeric mode. The characters are drawn with vectors and the smallest character size may be difficult to read because of the smaller size of the 305 screen, and the correspondingly smaller characters,

as compared to the Tektronix 4014 terminal. Also, the size and/or shape of the Tektronix-mode characters will change when the x-y gains are changed in the native mode. This allows the character size to remain proportional to the image size and allows oversized characters to be drawn.

3. Valve Leakage Monitoring

On November 29, 1984, a meeting was held at the Rockwell International Energy Technology Engineering Center (ETEC), Canoga Park, CA, with attendees from ETEC, ANL, ORNL, and NRC. The purpose of the meeting was to discuss the possibility of integrating ANL and ORNL into the NRC-funded valve leakage program at ETEC. The participants viewed the facilities and proposed site for the valve leakage experiments. A cooperative program, in which useful acoustic leak data would be obtained from a variety of valves, seems feasible. A comparison between ANL crack leak data and valve leak data obtained with ANL instrumentation would provide useful input to the problem of discriminating valve leaks from crack leaks.

C. Technical Progress in NDE

1. Informal Workshop on NDE of Pipes with Weld Overlays

a. Background

An NDE workshop on inspection of 12-in. Schedule 80 pipe-to-elbow weldments with weld overlays, from the Georgia Power Co. Hatch-2 reactor, was held at ANL in May 1984.[1] Because of the positive response to this workshop, a second one was held at ANL in January 1985. The ten participants included personnel from KWU (West Germany), Commonwealth Edison, Battelle Pacific Northwest Laboratory (PNL), Southwest Research Institute, and ANL. Two pipe-to-endcap weldments with weld overlays, also from Hatch, were studied in the second workshop. Figure 6 shows the dimensions and configurations of these weldments. The endcap is intact on weldment 22BM, a photograph of which is shown in Fig. 7. The center of the weld is marked and circumferential positions are indicated every 5 cm for reference. The inner surfaces of the weldments have been ground in some areas so that they contain a mixture of smooth areas and areas where the weld root is clearly evident (see Fig. 8). The weld overlay has a relatively smooth surface texture. The specimens were slightly radioactive, but the level was so low (less than 0.2 mr/hr) that no time or clothing restrictions were necessary for the workshop participants. The low radiation level was achieved by decontamination procedures carried out by Quadrex Corp. Part of the decontamination procedure involves an electropolishing process.

Before they were shipped to ANL, the weldments were sent to the J. A. Jones NDE Center in Charlotte, NC, where they were inspected by dye penetrant, ultrasonic, and radiographic techniques. Ultrasonic and radiographic techniques were difficult to apply to these weldments, but penetrant testing (PT) of the inner surface did reveal a limited amount of cracking in specimen 22BM. No crack indications were observed in specimen 22AM. Figure 9 shows the PT indications obtained in a region of 22BM ex-

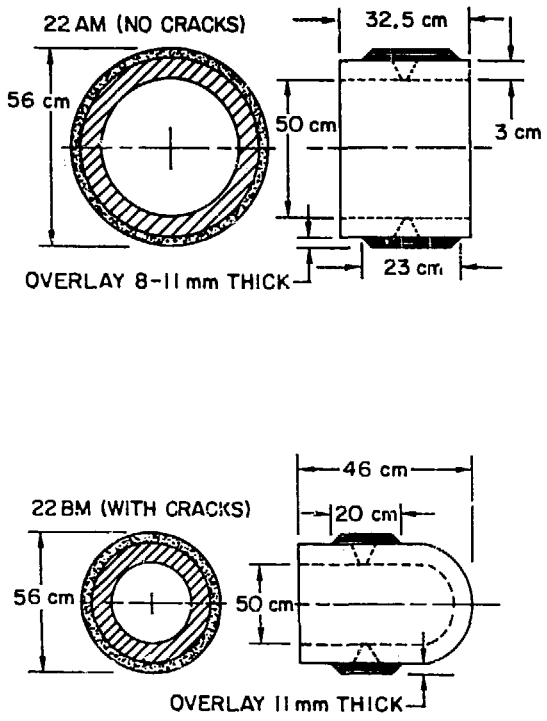

Fig. 6. Schematics of the Two Pipe-to-Endcap Weldments Used in the 1985 NDE Workshop.

Fig. 7. Photograph of Weldment 22BM.

tending from 129 to 137 cm. These cracks were also detected by PT at ANL. Figure 10 shows some additional PT results. Because of the limited amount of cracking in these weldments, the emphasis of the workshop was on trying to understand the nature of crack overcalling and the distortion of ultrasonic waves due to the presence of the overlay.

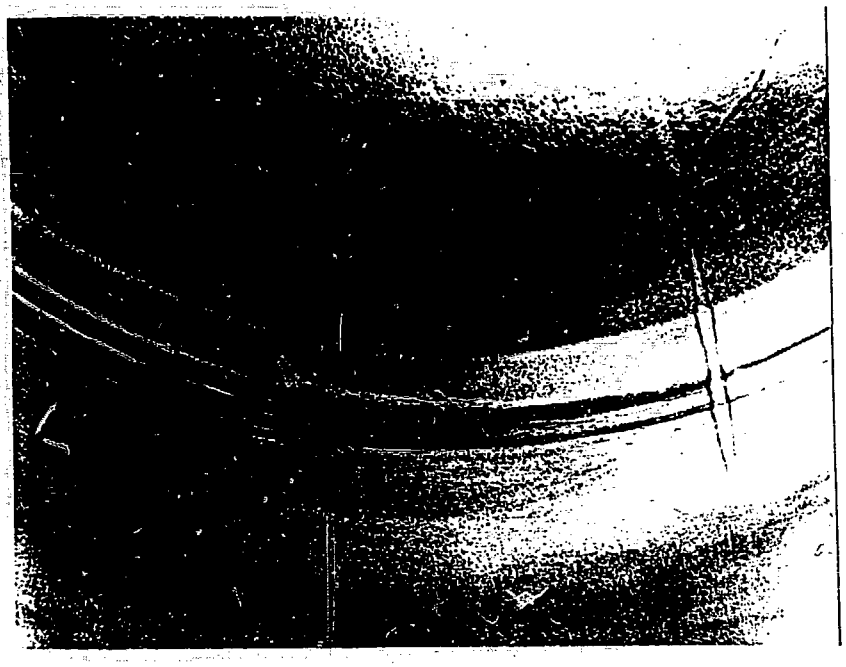

Fig. 8. Photograph of Inner Surface of 22BM Weldment, Showing Contrast Between Smooth Area (Ground) and Area with Prominent Weld Root (Unground). Dye-penetrant IGSCC indications are also evident.

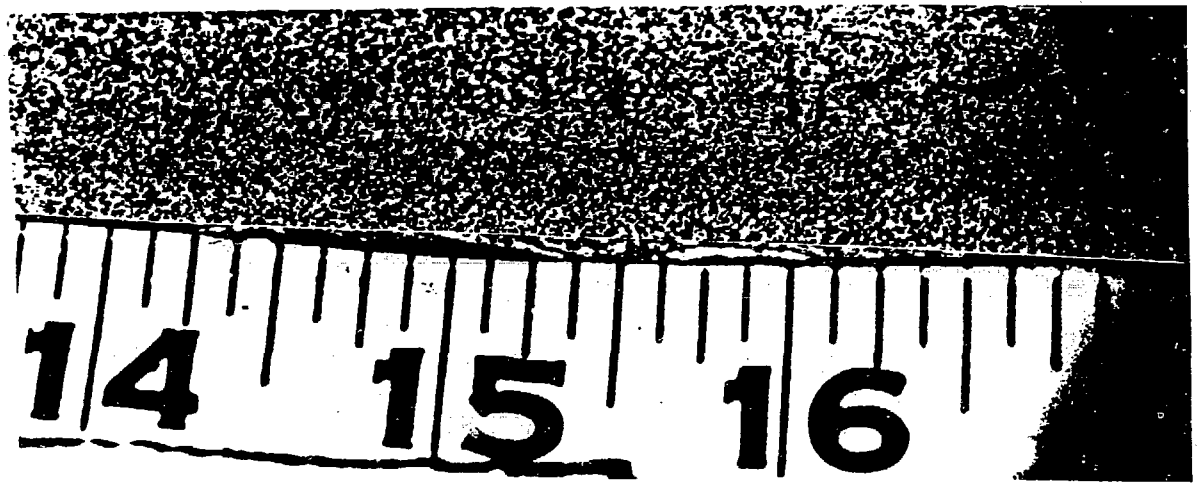

Fig. 9. Dye-Penetrant Indications Obtained by J. A. Jones in the 129-to-137 cm Region of Specimen 22BM.

Fig. 10. ANL Photograph of Outer Surface of Weldment 22BM After Dye-Penetrant Examination. Short inked lines just below the weld centerline show positions of small inner-surface cracks in the 130-to-150 cm region.

b. Group Discussion

A general discussion on the difficulties of inspecting weld overlays was held on one of the days when all participants were present. The presence of both field inspectors and researchers resulted in an informative exchange of ideas. The statements below summarize the main conclusions drawn from this discussion.

- The ISI of piping with an overlay is unreliable for cracks that extend less than ~60% throughwall because of the unpredictable beam distortion due to the overlay (which can vary considerably in size and thickness from one weld to another) and the absence of effective reference pipes. Optimization of the inspection procedure will require documentation of the overlay procedure and the availability of reference mock-up pipes. These reference pipes should have reflectors in both the heat-affected zone (HAZ) and the weld root. Field pipes removed from service are the most desirable.

- It is particularly difficult to separate crack signals from root signals when inspecting pipes with overlays because of the low signal-to-noise (S/N) ratio. It may be possible to improve the chance of detecting large cracks (>60% throughwall) through use of longitudinal waves (L-waves) and transducers with lower frequencies, although this will reduce the sensitivity to small cracks (less than 20% throughwall).

• Many ultrasonic echoes are seen while inspecting the endcap welds. A large fraction should be identifiable as due to geometrical reflectors from their dynamic characteristics as the transducer is moved.

• A baseline ultrasonic examination, performed with automated equipment, would be extremely useful as one could re-examine the pipe from time to time and look for changes resulting from crack initiation and growth. Automation makes this procedure feasible.

• The advantage of L-waves over shear waves for inspection of pipes with overlays is that L-waves undergo minimal attenuation and skewing while propagating through the overlay (or butt weld). It is also easier to see a crack tip signal with L-waves. The disadvantage is that the relative energy reflected back from a corner reflector is less than for shear waves.

• These endcap weldments were harder to inspect than the samples of 12-in. piping used in the previous workshop.[1]

Other comments made during the general discussion were as follows: (a) Cracks tend to blunt when an overlay is put on; this makes it easier to see the crack tip. (b) Replacement pipes (316 NG SS) may have large grains in the HAZ, which make ultrasonic testing (UT) more difficult than for 304 SS. (c) Deep cracks that are present before the overlay is applied can be located again by UT after overlaying. (d) It may be easier to detect deep cracks that follow the fusion line by inspecting with L-waves through the weldment, because the crack face may then be nearly perpendicular to the beam. Overall, L-waves would be favored for pipes with an overlay. (e) In principle, it may be advantageous to employ horizontally polarized shear waves (SH-waves) rather than the conventionally used vertically polarized shear waves (SV-waves). Beam distortion would be minimized, and relatively strong reflections would be generated at the intersection of the crack with the inner pipe surface. In practice, however, it would be difficult to generate these waves, and a change in the columnar grain structure would cause the wave to split into both SH- and SV-waves. (f) Two of the participating organizations are currently studying beam distortion in weld overlays. KWU is using electromagnetic acoustic transducers to map the beam; ANL is using a laser interferometer (see Section C.2.b below).

c. Experimental Results

A number of ultrasonic probes were used during this workshop. They included pitch-catch (side-by-side and tandem) and pulse-echo modes with both longitudinal and shear angle beams. Longitudinal beam angles of 45, 55, and 70°, and shear beam angles of 45 and 60°, were used. A special probe that mode converts a shear wave into a surface-skimming bulk wave at the inner surface was also tried. Transducer frequencies ranged from 1 to 3 MHz with sizes ranging from 6 to 25 mm. USIP 11, USL 48, and Panametrics 5052 UAX pulser-receivers were employed during the laboratory investigation to allow analysis of both radio frequency and video signals.

By means of the finger damping technique, many ultrasonic echoes could be identified as originating from the weld root. However, signals of unknown origin were detected at several transducer positions. These positions were carefully marked on the weldments; several examples are seen in the lower half of Fig. 10, where crosses labeled "L" and "S" show beam entry points for L-waves and shear waves, respectively. Examples of these difficult-to-classify echoes are shown in Figs. 11 and 12. Figure 12 (top) shows an echo obtained with a 2-MHz, 55° L-wave pitch-catch transducer at the 150-cm position of weldment 22BM. This signal is about 8 dB lower in magnitude than a signal from a known IGSCC in a section of 28-in. pipe removed from service. Figure 11 (bottom) shows the ultrasonic echo obtained from the same region (see Fig. 10) with a 2-MHz, 45° shear wave transducer. This echo, which has a favorable S/N ratio, does not come from the weld root. Figure 12 shows results for the same two transducers at the 138-cm position. Neither echo in Fig. 12 can be identified as arising from the weld root.

d. Future Efforts

Destructive analysis of the weldments in regions where the origin of the echoes is not clear will be used to help identify the source of those signals. Results of the destructive analysis and correlation with ultrasonic echoes will be presented in the future. The analysis of selected regions of the weldments will include an evaluation of the microstructure and its anticipated effect on beam distortion. An attempt will be made to trace the ultrasonic beam from its entry point to locate the origin of echoes of interest. The depths of the small cracks detected by PT will be established to help estimate the size of the smallest detectable crack in a pipe with an overlay. The laser interferometer (see Section C.2.b) will also be used to evaluate distortion of the beam after propagation through the overlay. The weldments will be sectioned to preserve areas that could eventually be used for reference pieces. Some of these will be notched both in the HAZ and in the weld root. Ultimately, these reference sections could be made available to other laboratories.

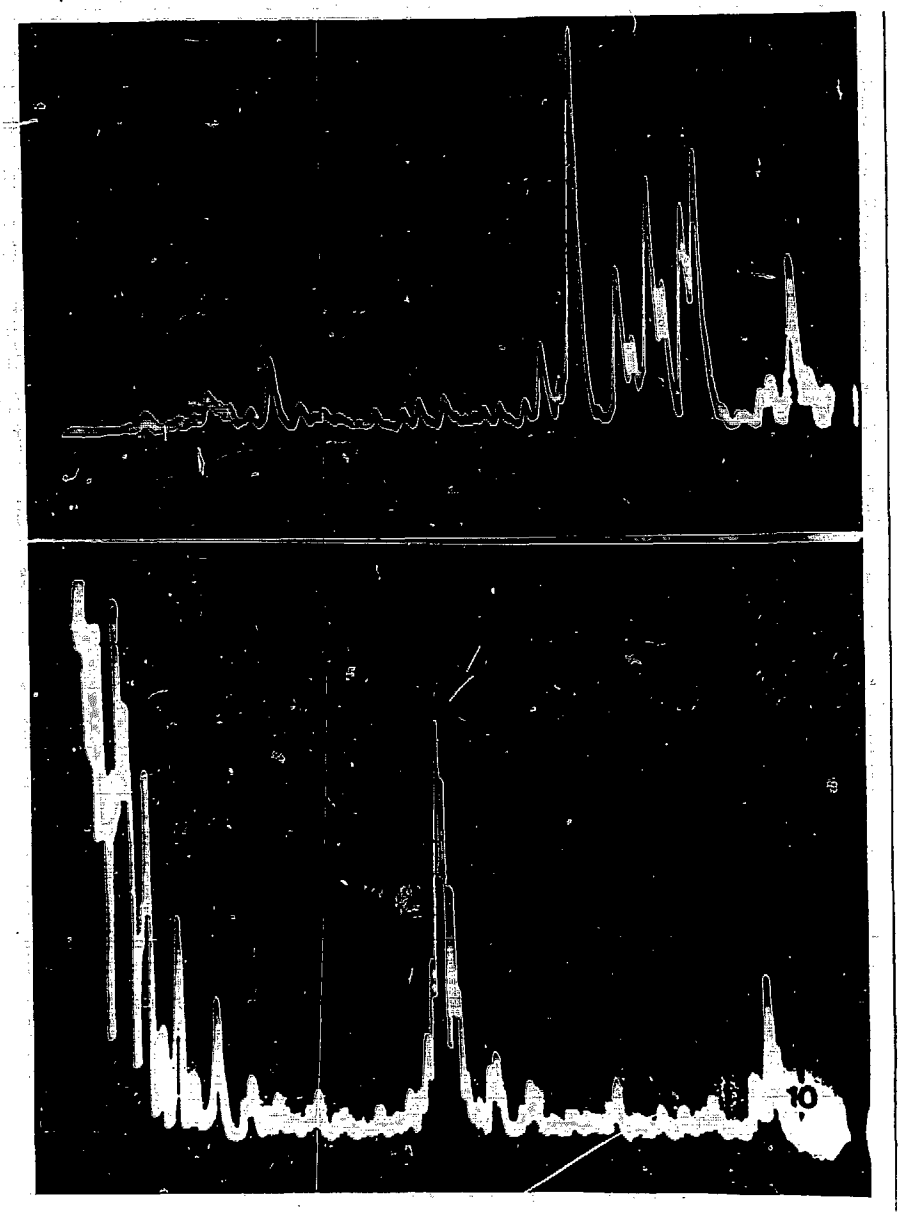

Fig. 11. Ultrasonic Echoes Obtained from Weldment 22BM with Transducers at ∿150-cm Position. (Top) 2-MHz, 55° L-wave pitch-catch transducer; (bottom) 2-MHz, 45° shear-wave transducer. The shear-wave echo is not a weld root reflection, and PT revealed no cracks at this location.

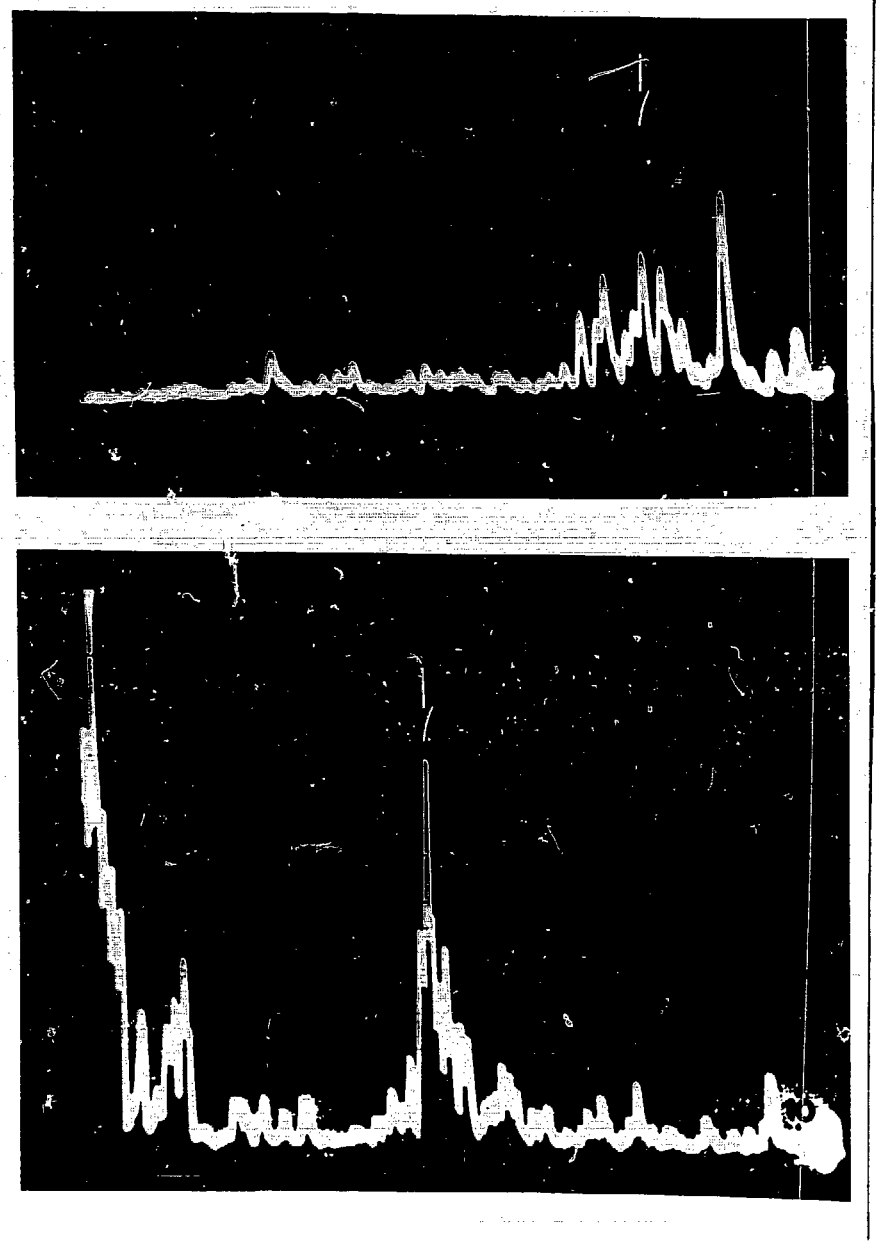

Fig. 12. Ultrasonic Echoes Obtained from Weldment 22BM with Same Transducers as Fig. 11, at ∿138-cm Position. Neither echo is from the weld root.

2. Ultrasonic NDE of Cast Stainless Steel

a. Ultrasonic Characterization of Microstructure

Although the ASME code requires the inspection of CSS piping in nuclear reactors, it has not been possible to demonstrate unambiguously that current inspection techniques are adequate. Ultrasonic inspection is difficult because the microstructure of CSS can vary considerably, from elastically isotropic with equiaxed, relatively small grains to elastically anisotropic with a columnar grain structure to a combination of the two.[1] For the near term, improvements that may increase the reliability of ultrasonic inspection include (a) the development of methods to establish the microstructure of the material (to help optimize the inspection technique), (b) the identification of calibration standards that are more representative of the material to be inspected, and (c) the use of cracked CSS samples for training purposes. For the long term, it will be necessary to establish (a) the variability of the microstructure of CSS both within and between components; (b) the effect of microstructure on inspection reliability; (c) the degree of improvement possible with techniques and equipment designed specifically for CSS, e.g., focused transducers and lower frequencies than those used conventionally; and (d) qualification requirements for CSS inspections.

The effect of microstructure on crack detection has been demonstrated with a 60-mm-thick CSS specimen provided by PNL. The specimen consists of two halves welded together (see Fig. 13). One half has an equiaxed grain structure; the other is columnar. The specimen contains a thermal-fatigue crack near the middle of the weld root. Details of the microstructures of this specimen are presented in Ref. 2.

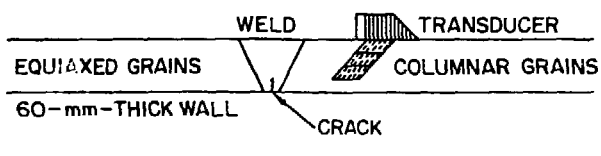

Fig. 13. Schematic of CSS Specimen Supplied by PNL. One side has equiaxed grains, the other columnar (vertical) grains. A thermal-fatigue crack was grown by PNL near the middle of the weld root.

The crack was detected from both sides of the weld with 0.5-MHz, 45° SV-waves in a pulse-echo mode and with 1-MHz, 45° L-waves in a pitch-catch (side-by-side) configuration. (The pitch-catch probe was provided by NRC Region 2 personnel.) At these frequencies, the wavelengths of the two interrogating beams are about the same. Thus, the effect of differences in Rayleigh scattering is minimized and variations in S/N ratios result from variations in beam distortion effects (for example, focusing of 45° L-waves in the columnar structure). The measured S/N ratios are shown in Table 2. For equiaxed grains, SV-waves gave a higher S/N ratio than L-waves. For the columnar-grain structure, the L-waves gave a higher S/N ratio. These data support our earlier conclusion[3] that knowledge of microstructure is important in optimizing the inspection of CSS.

TABLE 2. Signal-to-Noise Ratios[a] for Ultrasonic Echoes from Thermal-Fatigue Crack in CSS Specimen

Transducer Location (see Fig. 13)	Transducer: 45° SV 0.5 MHz 1x1 in. Pulse-Echo	Transducer: 45° L 1.0 MHz (focused) 1x1 in. Pitch-Catch
Columnar (Anisotropic) Side	3.5:1 (2 dB)	6:1 (8 dB)
Equiaxed (Isotropic) Side	7:1 (4 dB)	3:1 (2 dB)

[a]Numbers in parentheses are relative signal amplitudes.

Several specimens of CSS with varying microstructures (courtesy of O. Chopra, ANL) were examined to determine how well the structures could be characterized by ultrasonic techniques. The specimens are described in Table 3. The microstructures vary considerably, as shown in the optical micrographs of Fig. 14. Samples 69 and 75 are relatively fine grained. Sample 73 has relatively long columnar grains; the long axes of these grains are, for the most part, nearly perpendicular to the top of the plate (top of photograph), which would be the outer surface if it were a pipe. However, the columnar-grain axes tend to curve away from this orientation near the center of the plate. Passing sound through the thickness of these samples (top to bottom of photograph) simulates passing normal-incidence sound waves through a pipe wall.

TABLE 3. Characteristics of CSS Plate Specimens

Specimen	Material	Ferrite Content (%)	Dimensions (mm)
68(1)	CF-8	19	135 x 135 x 57
69(1)	CF-3	--	135 x 55 x 57
69(2)	CF-3	--	465 x 55 x 57
70(1)	CF-8M	16	192 x 170 x 57
70(2)	CF-8M	16	465 x 55 x 57
70(3)	CF-8M	16	590 x 180 x 67
73(1)	CF-8	7	600 x 170 x 67
75(1)	CF-8M	27	595 x 175 x 67

In the beam skewing technique, a 45° pitch-catch SV angle-beam probe is placed on the surface of a plate, and the distance between the two transducers is varied to determine the separation that gives the maximum received signal when the ultrasonic wave is reflected off the bottom of the

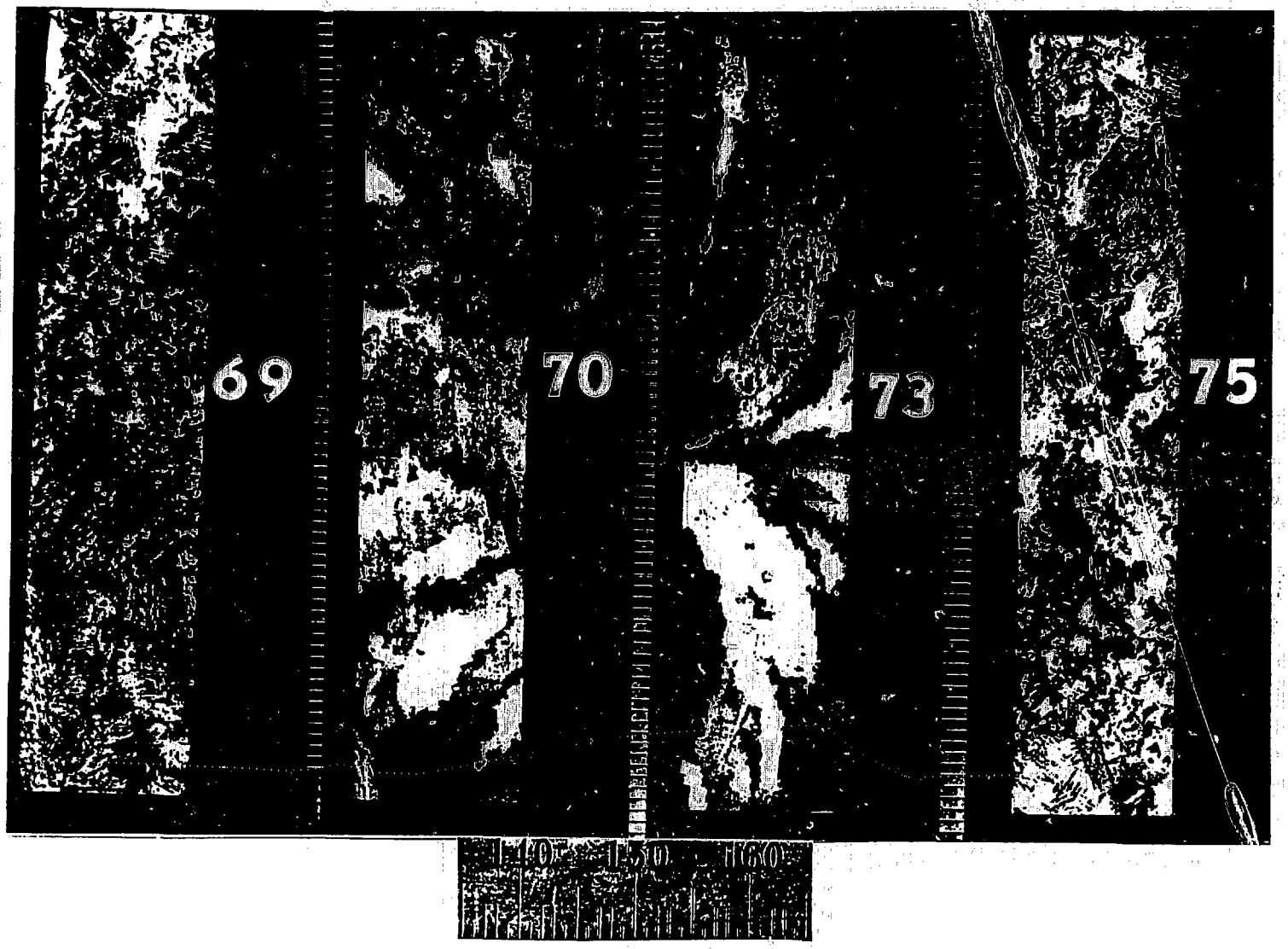

Fig. 14. Micrographs of Plates 69, 70, 73, and 75 (see Table 3). Top surface of each plate is at top of photograph.

plate. Because of the size and frequency of the transducers used (0.5 MHz, 1 in.), the beam undergoes considerable spreading (formation of "side lobes")[4], as shown in Fig. 15. Thus, in addition to the primary 45° SV-wave (solid diagonal lines in Fig. 15), there are also less intense SV-waves at steeper and shallower angles (dashed lines). If part of the wave propagates at an angle of incidence of about 21°, it can mode convert to a 45° L-wave at the back wall. With the transducers operating in the pitch-catch mode on a 60-mm-thick plate of isotropic SS, a weak SV-L wave signal should be received at a transducer separation of <120 mm, and a strong SV-SV wave signal at ∿120 mm. These waves can be identified on the oscilloscope trace by noting the transit times. When this probe configuration is used on anisotropic material, the transit time for a given wave type is approximately the same as in isotropic material, but the SV-SV wave is skewed more than the SV-L wave.[5] Consequently, the difference between the transmitter-receiver separations required for detection of maximum SV-SV and SV-L signals is smaller for anisotropic material.

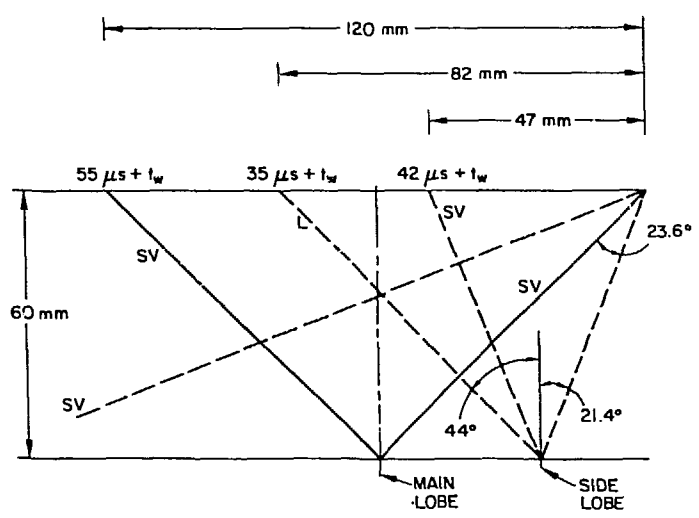

Fig. 15. Schematic Diagram Showing the Main and Side Lobes of a 1-in., 0.5-MHz 45° SV-Wave Probe and Resulting Mode-converted Beams After Reflection Off the Sample Bottom.

The following procedure was employed to test this concept. The transmitting transducer was placed on the top surface of the plate about 2 cm from one end; the receiving transducer was moved to maximize the SV-SV and SV-L received signals, and the separation was noted. The transmitter was then moved in ∿5-cm increments along a line parallel to the long edge of the plate, either near the edge or at the midline, and the procedure was repeated at each position; up to three experimental determinations were made at each position. Data were taken in this manner for plates 69, 70, 73, and 75 (at 9 or 11 positions each, depending on plate size). The results are shown in Fig. 16. For anisotropic material, the difference between the separations for maximum SV-SV and SV-L signals should be smaller than for isotropic material, since the SV-wave is skewed further back toward the transmitter

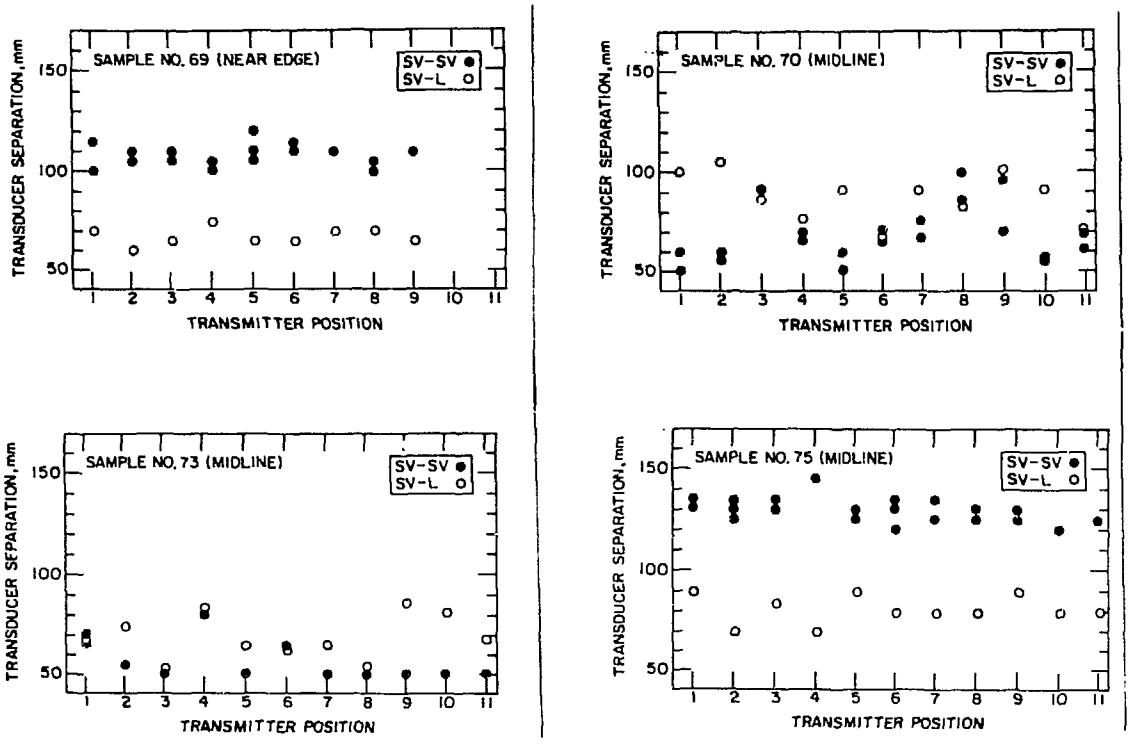

Fig. 16. Pitch-Catch Transducer Separations Giving Maximum Received SV-SV and SV-L Signals for Samples 69, 70, 73, and 75. Two 1-in., 0.5-MHz 45° shear-wave transducers were used. Successive transmitter positions (shown on x axis) are 5 cm apart.

than the L-wave, as previously discussed. This appears to be the case for sample 73, which, as shown in Fig. 14, has the most predominant columnar-grain structure. There is, however, considerable variation in the data. Samples 75 and 69 have the widest separation of SV-SV and SV-L waves (Fig. 16) and appear to have the finest texture (Fig. 14). Sample 70 has a coarse but ill-defined grain structure and gives the type of transducer separation data that one might expect for such a material; i.e., considerable point-to-point variation is observed in the separation between SV-SV and SV-L waves. Note that for sample 75, which is 67 mm thick, the transducer separation is about 120-140 mm for maximum SV-SV signals and 70-90 mm for maximum SV-L signals; these ranges agree with what one might expect for an isotropic crystal structure.

The sound velocity in a material may also serve as an indicator of anisotropy. One approach is based on the observation that CSS grain structure affects the velocity of L-waves and SV-waves differently. In the case of L-waves, velocity is lower for propagation parallel to the columnar-grain axis in anisotropic CSS than for propagation in isotropic (equiaxed) CSS. Conversely, for SV-waves, velocity is higher (although still lower than L-wave velocity) for propagation parallel to columnar grains than for propa-

gation in isotropic CSS. Thus, the ratio between L-wave and SV-wave velocity in a given CSS sample can serve as an indicator of anisotropy. Under ideal conditions, an anisotropic sample with sound waves propagating parallel to the columnar-grain axis will give an L/SV velocity ratio of about 1.4 (V_ℓ ∿5400 m/s, V_{SV} ∿4000 m/s). However, the ratio for an isotropic (equiaxed) structure would be about 1.74 (V_ℓ ∿5940 m/s, V_{SV} ∿3410 m/s).[1,2]

Figure 17 compares the L/SV velocity ratios for samples 70(3), 73(1), and 75(1) at 11 different points. Sample 75 (which is highly isotropic) has a ratio of about 1.8, in agreement with predictions, whereas sample 73 (with columnar grains oriented perpendicular to the surface except at a small region in the center, as seen in Fig. 14) has a ratio that varies from 1.8 at the ends to 1.6 away from the ends. Because of the heat flow during the fabrication process, the ends of a CSS plate are expected to have a different microstructure from the rest of the plate. For sample 70, with the coarse but ill-defined grain structure, the ratios range from 1.6 to 1.9 without any well-defined pattern.

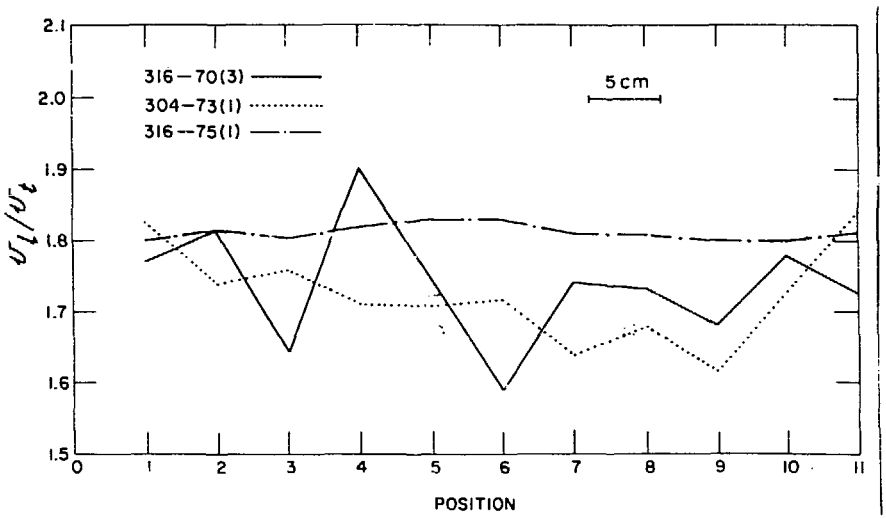

Fig. 17. Ratio of Normal-Incidence L- and SV-Wave Velocities for CSS Samples 70(3), 73(1), and 75(1) at 11 Different Transducer Positions.

Information about the microstructure can also be obtained from the L-wave velocity alone. As mentioned above, the L-wave velocity should be low for anisotropic material (if propagation is parallel to the grains) and high for equiaxed material. Figure 18 shows the longitudinal velocity of sound for samples 70(3), 73(1), and 75(1). The low velocity of sample 73 away from the ends of the plate implies a columnar structure, consistent with the micrograph of Fig. 14. The relatively high and constant values for sample 75 suggest fine, equiaxed grains, also consistent with the micrograph of Fig. 14. Finally, sample 70(3) shows large variations in velocity, suggesting an ill-defined, coarse grain structure not inconsistent with Fig. 14.

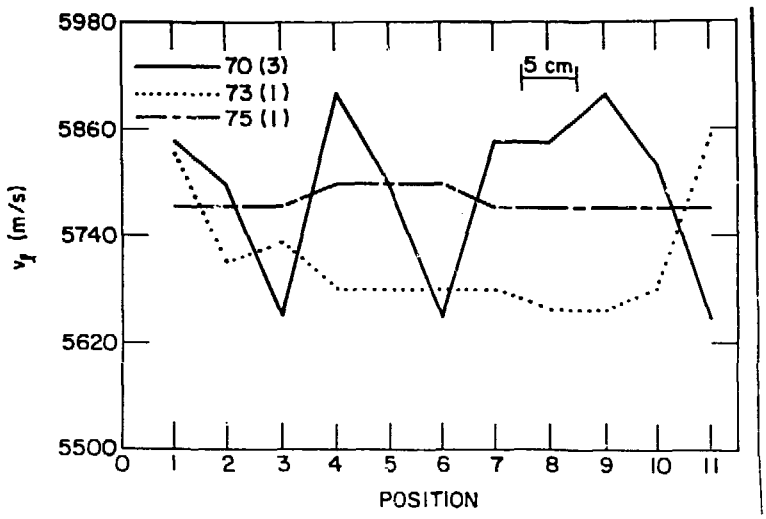

Fig. 18. Normal-Incidence Longitudinal Velocity of Sound for Samples 70(3), 73(1), and 85(1) at 11 Different Transducer Positions.

It appears that under laboratory conditions, ultrasonic velocity and pitch-catch echo amplitude measurements can be used to correctly predict the microstructure of CSS. Further efforts will be directed toward determining which of the techniques described here would be most effective under field conditions.

b. Visualization of Ultrasonic Beam Distortion

Laser detection of ultrasonic waves is becoming a popular method for applications where noncontacting measurements must be made or where high spatial resolution or quantitative measurements of displacement are required.[6-8] A laser interferometric technique was used to map the ultrasonic displacement profile from a transducer beam that had propagated through centrifugally cast stainless steel pipe wall material. The laser interferometer was calibrated by a direct capacitance method, which allowed quantitative measurement of the surface displacement amplitude to 0.35 Å.

The laser interferometer, shown schematically in Fig. 19, is a Michelson quadrature interferometer manufactured by Sonoscan.[9] The advantages of this system are good sensitivity (~0.3 Å) compared with other optical methods; ability to detect short (<1 μs) pulses; and insensitivity to low-frequency (f < 100 kHz) vibrations. The disadvantages of the system are that the signal voltage output is proportional to the square of the displacement and the apparent frequency of the waveform is doubled owing to the electronic stabilization technique. The system has a frequency band pass (-3 dB) of 150 kHz to 8 MHz, limited at low frequencies by laser noise and random vibrations and at high frequencies by the frequency response of the squaring and summing electronics. Because the sensitivity of the interferometer is proportional to the light intensity reflected from the surface to the photo-

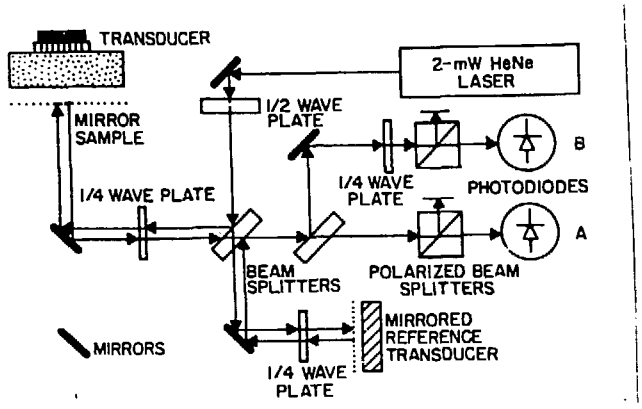

Fig. 19. Layout of the Optical Components for the Laser Interferometer.

diodes, a flat mirror-like sample surface is required for maximum sensitivity over the scanning area. As shown in Fig. 19, the sample, with the ultrasonic transducer affixed to the opposite face, is scanned in the x-y plane with mechanical stepping motors. Data were obtained at 760-μm increments with a beam diameter of 800 μm. (The beam could have been focused to a much smaller spot size, but the larger spot size made the technique less sensitive to surface scratches or imperfections.) The scan area was approximately 1.7 x 1.5 cm. During the scan, data from the interferometer were digitized and stored for normalization and plotting.

As the sample moves in front of the laser beam, changes in reflectivity occur as a result of scratches and misalignment of the sample surface. A normalizing signal at 2 MHz is applied to a piezoelectric crystal (mirrored reference transducer) in the reference arm, which provides a signal proportional to the surface reflectivity. This signal is then used to correct the amplitude of the signal received through the sample. This procedure eliminates asperity in the plots of the ultrasonic wavefront and allows measurement of small changes in amplitude.

Quantitative measurement with the interferometer requires that the laser system be calibrated. The system can be roughly calibrated by use of the relation between the photodiode current, i_s, and the light intensity in the reference arm and sample arm, I_r, I_s, as shown below.

$$i_s = 8\pi\eta \frac{(I_r I_s)^{1/2}}{\lambda} \delta \sin(\omega t), \qquad (1)$$

where δ is the displacement and η is the quantum efficiency of the photodiode. Use of Eq. (1) implies that the photodiode current, light intensity, and quantum efficiency are known or can be measured accurately. Even if this were the case, the transfer function for the rest of the laser system electronics would have to be measured. To circumvent the difficulty of calibrating each individual component, a calibration device was constructed.[10] The calibration device directly measures the time-dependent displacement of a mirrored fused-quartz surface.

A cross section of the calibrator is shown in Fig. 20. A wideband (1.9-cm-diam) piezoelectric transducer, epoxied to a fused-quartz block (2.5 cm thick x 3.8 cm diam), is used as a source of 0.5-2 MHz L-waves. The L-wave pulses, after propagating through the fused quartz, are reflected off the end of the quartz block, with resultant oscillatory surface displacement. The end of the fused-quartz block is sputtered with a mirror-like layer of chrome 2500 Å thick. A small (1.27-cm-diam) SS electrode measures the average change in capacitance over the surface due to the displacement. A 1-mm-diam hole in the center of the electrode allows the laser beam to measure the displacement at the center of the rear surface of the fused-quartz block. To calculate the peak-to-average displacement factor (<5%), the shape of the nearly Gaussian ultrasonic-beam wavefront was determined by scanning the laser over the back surface of the fused-quartz block with the capacitor electrode removed. Comparing the square root of the laser system output with the displacement as measured with the capacitor gave a sensitivity of 2.5×10^{-4} Å/Hz$^{1/2}$, or 0.35 Å sensitivity in a 2-MHz bandwidth. This is approximately the sensitivity for other reported Michelson-type interferometers.[6-8] This sensitivity is much less than that obtained with wideband piezoelectric probes such as the NBS acoustic emission sensor.[11] A comparison of the spectral sensitivities of the laser and the NBS conical transducer at 1 MHz indicated that the laser system is 47 dB less sensitive.

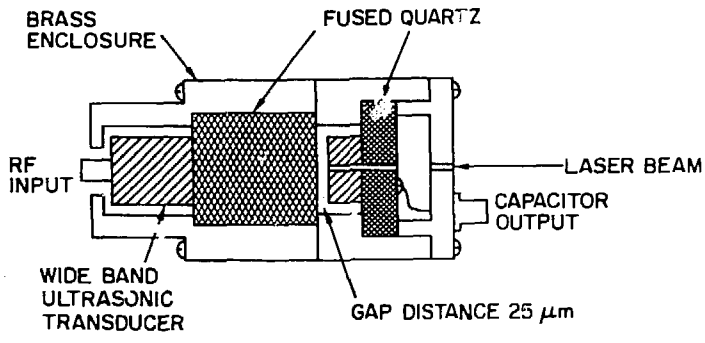

Fig. 20. Cross Section of the Capacitor Calibrator for the Laser Interferometer.

An increase in the sensitivity of the laser probes could be obtained with lower noise preamplifiers or photodiodes. The predominant noise in the laser system was found to be the thermal noise inherent in either the photodiode or preamplifier. A higher power (25-mW) HeNe laser was used with the system to improve the sensitivity by a factor of 5. With these and other improvements in the interferometric sensing system, it should be possible to achieve detection sensitivities comparable to that of wideband piezoelectric probes.

As shown in Fig. 19, a small, 6.3-mm-OD L-wave transducer was epoxied to various specimens of isotropic or transverse isotropic SS. Figure 21 shows etched surfaces of samples with (a) isotropic grains and (b) transverse isotropic grains with the grain axis oriented in the <100>

direction (confirmed by ultrasonic velocity measurements). Figure 22 shows a beam wavefront from the 6.3-mm transducer after passing through a 3.1-mm-thick sample of isotropic steel with grains less than 100 μm in diameter. The beam shape is approximately Gaussian and symmetric about the center of the transducer. Note that the center of the transducer does not, in general, coincide with the center of he scan area of the three-dimensional plot.

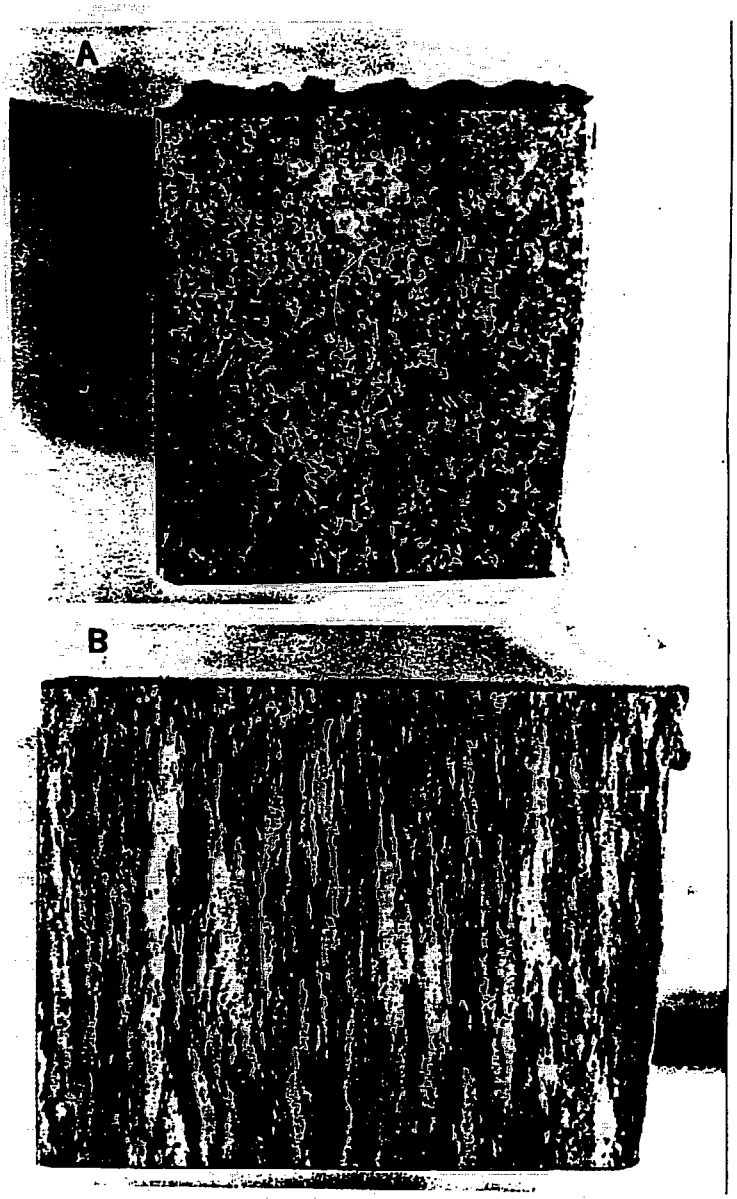

Fig. 21. Etched Cross Sections of Austenitic SS Samples Showing (a) Isotropic Grain Structure and (b) Columnar Grain Structure.

In addition, because of the perspective for Fig. 22, the contour plot looks elliptical rather than circular. The plots were constructed by pulsing the transmitting transducer with a 200-V, 0.2-μs unipolar pulse and subsequently detecting the peak laser signal at 2 MHz as a function of position and then converting to peak displacement in angstroms.

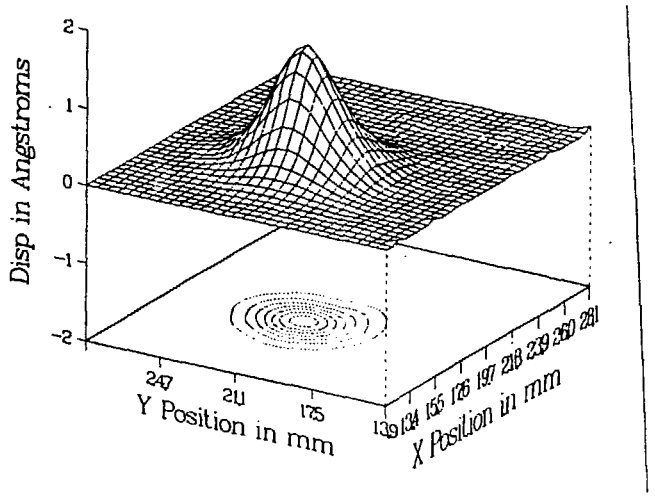

Fig. 22. Displacement of L-Waves from a 6.3-mm-diam Transducer Mounted on the Back Surface of a 3.1-mm-thick Isotropic Austenitic Steel Sample.

Several thicker samples with longer grains (2-3 mm diam x 1 cm in length) were also tested. In Fig. 23, beam wavefronts originating from the 6.3-mm transducer are shown after passing through 19 mm of centrifugally cast austenitic steel. Figure 23a shows the wavefront for the longitudinal beam incident at a 45° angle to the grain axis. The beam should not be skewed by any significant amount but should be focused in the y direction indicated on the graph. This focusing effect results in an elliptical shape of the beam at the backwall.[12,13] A calculation of the spreading of the beam as described in Ref. 13 gives a beam diameter of 15 mm for an amplitude decrease of 50%. The measured beam diameter in the x direction is about 13 mm for a 50% decrease in signal level. In the y direction, the beam has been focused down to 8 mm. The beam wavefront for L-waves traveling parallel to the axis of the grains is shown in Fig. 23b. In contrast to Fig. 23a, the beam has spread very little (3 mm diam for 50% decrease in amplitude), which is not the behavior predicted for propagation along the grain axis. This may be due to the relative sizes of the grains and transducer. Obviously, when the grains are 2-3 mm in diameter and the beam is 6.7 mm in diameter, only a few local grains are averaged by the beam, which may negate the observation of global transverse isotropy.

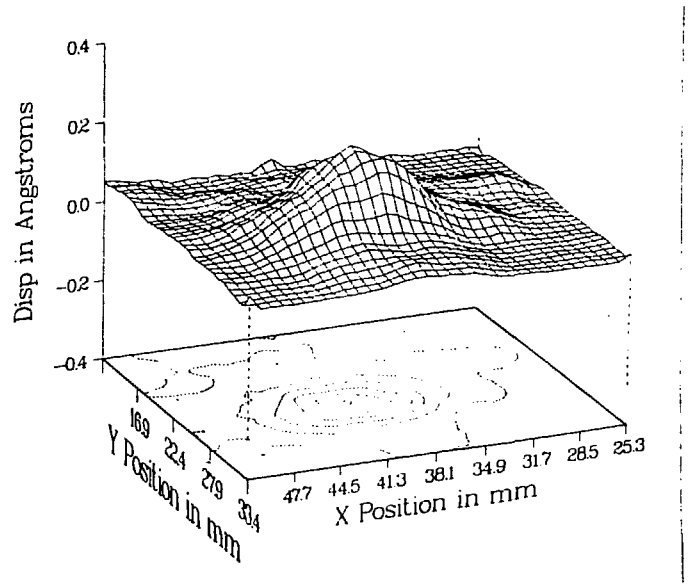

(a)

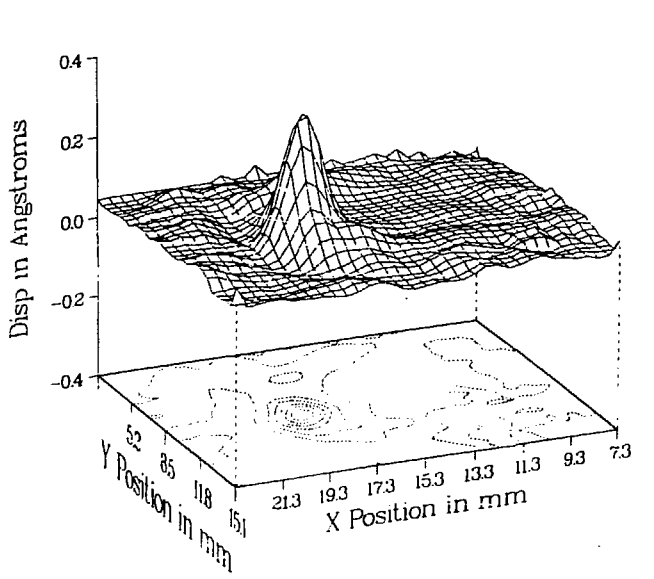

(b)

Fig. 23. Displacement of L-Waves from a 6.3-mm-diam Transducer Mounted on the Back Surface of a 19-mm-thick Austenitic Steel Sample with the Grains Oriented (a) at a 45° Angle to the Incident Beam and (b) Parallel to the Incident Beam.

ACKNOWLEDGMENTS

The authors wish to thank J. Abrego-Lopez, R. N. Lanham, and N. Scholtes for assistance in acquiring data presented in this paper. We also wish to thank K. J. Reimann for useful discussions and E. M. Stefanski for editing the manuscript.

REFERENCES

1. D. S. Kupperman, T. N. Claytor, and D. W. Prine, NDE of Stainless Steel and On-Line Leak Monitoring of LWRs: Annual Report October 1983-September 1984, Argonne National Laboratory Report NUREG/CR-4124, ANL-85-5, p. 15 (April 1985).

2. W. J. Shack et al., Materials Science Division Light-Water-Reactor Safety Research Program: Quarterly Progress Report January-March 1982, Argonne National Laboratory Report NUREG/CR-2970 Vol. I, ANL-82-41 Vol. I, p. 10 (October 1982).

3. W. J. Shack et al., Environmentally Assisted Cracking in Light Water Reactors: Annual Report October 1982-September 1983, Argonne National Laboratory Report NUREG/CR-3806, ANL-84-36, p. 39 (June 1984).

4. L. E. Kinsler and A. R. Frey, Fundamentals of Acoustics, John Wiley and Sons, New York (1950).

5. D. S. Kupperman, K. J. Reimann, and D. I. Kim, "Ultrasonic Characterization and Microstructure of Stainless Steel Weld Metal," in Nondestructive Evaluation: Microstructural Characterization and Reliability Strategies, ed. O. Buck and S. Wolf, The Metallurgical Society of AIME, New York, p. 199 (1981).

6. W. Sachse and N. N. Hsu, "Ultrasonic Transducers for Materials Testing and Their Characterization," in Physical Acoustics, Vol. XIV, ed. P. Mason, p. 277 (1979).

7. F. Nadeau and D. A. Hutchins, "A Study of Surface Waves with Slots Using Non-Contact-Laser Generation and Detection of Ultrasound," in IEEE Ultrasonics Symposium, Dallas, TX, p. 921 (1984).

8. C. H. Palmer and R. E. Green, Jr., Optical Detection of Acoustic Emission Waves, Applied Optics 16, 2333 (1977).

9. Sonoscan, 530 E. Green St., Bensenville, IL 60106.

10. J. H. Cantrell, Jr. and M. A. Breazeale, Elimination of Transducer Bond Corrections in Accurate Ultrasonic-Wave Measurements by Use of Capacitive Transducers, J. Acoust. Soc. Am. 61, 403 (1977).

11. T. Proctor, An Improved Acoustic Emission Transducer, J. Acoustic. Soc. Am. 71, 1163 (1982).

12. J. T. Thomson and J. M. Farley, "Ultrasonic Examination of Austenitic Welds: Theoretical and Practical Considerations," in 6th Intl. Conf. on Nondestructive Evaluation in the Nuclear Industry, Zurich, Switzerland, Am. Soc. for Metals, Metals Park, OH, p. 225 (1983).

13. D. S. Kupperman, K. J. Reimann, and D. Yuhas, "Visualization of Ultrasonic Beam Distortion in Anisotropic Stainless Steel," in 5th Intl. Conf. on Nondestructive Evaluation in the Nuclear Industry, San Diego, CA, Am. Soc. for Metals, Metals Park, OH, p. 172 (1982).